Impacts of subpixel cloud heterogeneity on infrared thermodynamic phase assessment

Brian H. Kahn,[1] Shaima L. Nasiri,[2] Mathias M. Schreier,[1,3] and Bryan A. Baum[4]

Received 3 February 2011; revised 19 July 2011; accepted 23 July 2011; published 18 October 2011.

[1] A combination of spatially collocated Atmospheric Infrared Sounder (AIRS) radiances and Moderate Resolution Imaging Spectroradiometer (MODIS) cloud products are used to quantify the impact of cloud heterogeneity on AIRS-based assessments of cloud thermodynamic phase. While radiative transfer simulations have demonstrated that selected AIRS channels have greater sensitivity to cloud thermodynamic phase in comparison to the relevant MODIS bands, the relative trade-offs of spectral and spatial resolution differences that are inherent between AIRS and MODIS have not been quantified. Global distributions of AIRS field-of-view scale frequencies of clear sky (13–14%), heterogeneous cloud (26–28%), and homogeneous cloud (59–60%) are quantified for a four week time period using cloud fraction, and further categorization of cloud uniformity is assessed with the variance of cloud top temperature. Homogeneous clouds with window brightness temperatures (T_b) between 250 and 265 K are shown to have larger cloud thermodynamic phase signatures than heterogeneous clouds. Clouds in this limited T_b range occur 30–50% of the time in the mid- and high latitude storm track regions, are generally difficult to identify as being water or ice phase, and show strong responses in forced CO_2 climate change modeling experiments. Two-dimensional histograms of T_b differences sensitive to cloud phase (1231–960 cm^{-1}) and column water vapor (1231–1227 cm^{-1}) show distinct differences between many homogeneous and heterogeneous cloud scenes. The results suggest the potential for a quantitative approach using a combination of hyperspectral sounders with high-spatial-resolution imagers, and their derived geophysical products, to assess cloud thermodynamic phase estimates within increasingly complex subpixel-scale cloud variability.

Citation: Kahn, B. H., S. L. Nasiri, M. M. Schreier, and B. A. Baum (2011), Impacts of subpixel cloud heterogeneity on infrared thermodynamic phase assessment, *J. Geophys. Res.*, *116*, D20201, doi:10.1029/2011JD015774.

1. Introduction

[2] Variability in climate sensitivity among climate model projections is primarily due to uncertainty about cloud feedbacks as a result of anthropogenic climate change. The cloud feedback response includes spatial and temporal changes in the frequency, vertical distribution, and microphysical and optical properties of the clouds as well as changes in the thermodynamic and dynamic structure of the atmosphere [*Schneider et al.*, 2010]. Modeling experiments with CO_2-induced warming [e.g., *Wetherald and Manabe*, 1988; *Mitchell and Ingram*, 1992; *Trenberth and Fasullo*, 2010; *Zelinka and Hartmann*, 2010] have shown that upper tropospheric clouds tend toward higher altitudes in the subtropics and tropics (positive cloud feedback), while low and middle tropospheric cloud frequency and water content increases in the high latitudes, causing greater shortwave reflectance (negative cloud feedback). Recent studies have shown that there exists a wide range of inter-model variability of subtropical and tropical boundary layer cloud amount in 21st century climate projections when compared to current observations [*Stephens*, 2005; *Williams and Tselioudis*, 2007; *Medeiros et al.*, 2008]. Improvements in the representation of low-latitude boundary layer clouds could significantly reduce cloud-climate feedback uncertainties [*Bony and Dufresne*, 2005].

[3] Despite the importance of low-latitude boundary layer clouds, the radiative implications of uncertainty in cloud phase (liquid, mixed-phase, and ice) are substantial [*Sun and Shine*, 1995; *Yang et al.*, 2003]. For example, *Mitchell et al.* [1989] and others have shown that a large variation of climate sensitivity is obtained in response to the treatment of cloud phase in CO_2 doubling experiments. *Senior and Mitchell* [1993] showed that a substantial increase in cloud water amount is observed in the "mixed phase" temperature range (0°C to −15°C) for a similar CO_2 doubling experiment.

[1]Jet Propulsion Laboratory, California Institute of Technology, Pasadena, California, USA.
[2]Department of Atmospheric Sciences, Texas A&M University, College Station, Texas, USA.
[3]Joint Institute for Regional Earth System Science and Engineering, University of California, Los Angeles, California, USA.
[4]Space Science and Engineering Center, University of Wisconsin-Madison, Madison, Wisconsin, USA.

0148-0227/11/2011JD015774

Since the ratio of liquid to ice cloud was shown to increase and *Senior and Mitchell* [1993] noted a greater temporal "persistence" of liquid compared to ice cloud, an increase in cloudiness in the mid- and high latitudes resulted in higher shortwave reflectance (negative cloud feedback). In another CO_2 doubling experiment, *Li and Le Treut* [1992] showed that a simple model parameter adjustment of the transition of liquid to ice cloud from 0°C to −15°C causes a vertical ascent of cloud in the low latitudes and a poleward migration of cloudiness in the mid- and high latitudes. Both effects are associated with positive feedback, the first because of increased IR trapping and the second because of reduced shortwave reflectance at lower sun angles, which compete with the negative feedback associated with increased water content. In a comparison of several climate models with doubled CO_2, *Tsushima et al.* [2006] showed that models with higher climate sensitivity produce smaller increases in cloud water amount than models with lower climate sensitivity. To diagnose the physical mechanisms of the cloud-climate response, *Ogura et al.* [2008] partitioned the terms of the nonconvective cloud condensate tendency equation in the MIROC 3.2 and HadGEM1 models. The zonal patterns of the cloud response closely resembled the response of the condensation-evaporation and deposition-sublimation terms, arguing for an explicit representation of competing microphysical processes in climate models, for instance, with bin microphysical parameterizations [e.g., *Morrison and Gettelman*, 2008].

[4] *Doutriaux-Boucher and Quaas* [2004] used POLarization and Directionality of the Earth's Reflectances (POLDER) retrievals of cloud phase to develop a statistical cloud phase technique that is incorporated into the Laboratoire de Météorologie Dynamique (LMD) GCM. Simulations using this statistical approach showed improvements in the shortwave forcing produced by the LMD GCM. Toward this end, a multiyear, global "best estimate" record of cloud phase, with sufficient spatial and temporal resolution to resolve small-scale process [e.g., *Naud et al.*, 2006], would offer a highly useful observational constraint for climate model evaluation. However, at present, large differences in the sensitivity, sampling, precision, and accuracy exist between various active and passive cloud phase detection approaches [*Goloub et al.*, 2000; *Chylek et al.*, 2006; *Nasiri and Kahn*, 2008; *Cho et al.*, 2008, 2009; *Hu et al.*, 2010; *Naud et al.*, 2010; *Riedi et al.*, 2010]. The largest discrepancies are in high latitudes where clouds are prevalent with temperatures between −40 and 0°C. For example, approximately 20–25% of all clouds globally are classified as "mixed" or "unknown" for the month of January 2005, according to the Moderate Resolution Imaging Spectroradiometer (MODIS [*Barnes et al.*, 1998]), but these percentages are much higher poleward of 40° [*Nasiri and Kahn*, 2008, hereinafter NK08; *Morrison et al.*, 2011].

[5] In the case of cloud phase determined from active profiling by the Cloud-Aerosol Lidar with Orthogonal Polarization (CALIOP [*Winker et al.*, 2010]), the greatest frequency of clouds in this temperature range is highest from 40–70° in both hemispheres, but approximately 95% of these clouds are identified as liquid [*Hu et al.*, 2010], much higher than passive estimates of cloud phase [*Jin et al.*, 2010]. Preliminary efforts to infer cloud phase with the Atmospheric Infrared Sounder (AIRS [*Aumann et al.*, 2003]) indicate that, between −30 and 0°C, AIRS generally classifies a lower percentage of clouds as liquid compared to CALIOP [*Jin et al.*, 2010]. While CALIOP has greater phase sensitivity than any existing passive satellite instrument, it also has some limitations. CALIOP is not a scanning instrument and therefore observations are only made along a narrow track. Additionally, the CALIOP data set is of limited duration, beginning in 2006 and without immediate plans for a follow-on mission at the end of the current instrument's lifespan. While the phase sensitivity of infrared instruments is lower, the AIRS data set is global and extends back to 2002. In addition, AIRS retrieves atmospheric temperature and humidity profiles along with cloud top temperature and effective cloud fraction, which makes is possible to relate clouds to the existing thermodynamic regime. Because it appears likely that high-spectral-resolution infrared sounders will be launched in the foreseeable future (e.g., CrIS and IASI), a long-term global IR cloud phase data set is possible.

[6] NK08 determined MODIS and AIRS sensitivities to cloud phase using 8–11 μm [*Strabala et al.*, 1994; *Baum et al.*, 2000] and 1231–960 cm^{-1} brightness temperature differences (ΔT_b), respectively, for a range of cloud top temperatures, optical thicknesses, and effective diameters. Although the hyperspectral simulations of AIRS ΔT_b showed a robust separation of liquid and ice for most single-layer cloud configurations that were not obtainable in the MODIS narrowband simulations, the trade-offs between spatial and spectral resolution were not investigated. The nominal spatial resolution of the AIRS footprint is 13.5 km at nadir, but cloud structure can vary at much smaller spatial scales; *Chylek and Borel* [2004] saw cloud phase variations at scales of 10s of meters. Small-scale cloud heterogeneity is also important for assessing deviations from plane-parallel cloud structure [e.g., *Cahalan et al.*, 1994; *Oreopoulos and Cahalan*, 2005; *Di Girolamo et al.*, 2010] and subsequent passive visible/near-infrared retrievals of cloud optical thickness and effective particle size [*Wolters et al.*, 2010]. Biases of several Kelvins in T_b and cloud top temperature, along with ~20% errors in cloud top emissivity, result from plane-parallel assumptions about heterogeneous clouds that resemble cubes or have aspect ratios on the order of 1.0 [*Liou and Ou*, 1979; *Harshvardhan and Weinman*, 1982; *Coakley et al.*, 2005]. Furthermore, in the mid-infrared spectral region, water vapor in the lower atmosphere impacts ΔT_b in the 8–12 μm window within clear, partially overcast, and transparent overcast conditions. This may cause spectral variations in ΔT_b for heterogeneous cloud cover that otherwise would not be present in homogeneous and opaque cloud cover located above most of the water vapor column.

[7] This study quantifies the impacts of cloud heterogeneity on cloud thermodynamic phase assessment at spatial scales smaller than the AIRS footprint using collocated MODIS cloud products. The coincident observations are spatially collocated using the method of *Schreier et al.* [2010]. Section 2 describes the data and methodology used in this study. Several AIRS channel combinations are exploited to highlight sensitivity to cloud thermodynamic phase, column water vapor, and cloud particle size. These are used in conjunction with cloud products from MODIS, whose variability within the AIRS field of view (FOV) is retained to quantify cloud thermodynamic phase sensitivity as a func-

tion of this variability. Section 3 presents statistical results of global distributions of cloud heterogeneity and homogeneity as viewed at the AIRS FOV. Section 4 outlines a set of simulations describing typical ΔT_b in clear skies for particular window channel differences of interest that are sensitive to cloud phase, particle size, and water vapor. The simulations help quantify ranges of ΔT_b that likely either contain cloud or potentially clear sky. Then, section 5 describes two-dimensional histograms of ΔT_b conditioned by cloud heterogeneity in the context of simulations presented in section 4. Histograms of ΔT_b are presented for a wide variety of "cloud types" that are characterized by scan angle and cloud heterogeneity using MODIS cloud fraction, cloud top temperature [*Menzel et al.*, 2008], and infrared cloud thermodynamic phase. In section 6, the findings in this study are summarized and the implications for using hyper-spectral infrared radiances for cloud thermodynamic phase assessment are discussed.

2. Data and Methodology

[8] The Aqua MODIS and AIRS pixel-scale observations are spatially combined following the methodology of *Schreier et al.* [2010] for four separate time periods: 1–6 January, April, July, and October 2005. Approximately 10–12 million oceanic AIRS IR FOVs are quantified for each time period in sections 4 and 5. The scan angle-dependent truncated, rotated, and smeared spatial response functions determined from AIRS prelaunch calibration are used to collocate the Collection 5 (C5) MODIS Level 1b and Level 2 derived products within each AIRS FOV. The collocation files preserve the AIRS FOV-scale variability and also help simplify the spatial averaging of MODIS properties to the AIRS FOV. The spatial averaging uses a weighting coefficient determined for each individual MODIS pixel that is a function of the magnitude of the AIRS spatial response. The 1 km C5 MODIS cloud mask (MYD35) [*Ackerman et al.*, 2008; *Frey et al.*, 2008] quantifies the AIRS FOV-scale cloud heterogeneity, while the 5 km C5 IR cloud phase mask ("Cloud_Phase_Infrared" in MYD06_L2) [*Platnick et al.*, 2003] determines the cloud phase of the MODIS pixels. Although it is anticipated that Collection 6 (C6) will have improvements in the IR phase from the use of cloud emissivity ratios [*Pavolonis*, 2010] and a higher spatial resolution of 1 km rather than 5 km, C6 operational products are not yet available. The MODIS cloud mask uses 19 of 36 MODIS bands and a variety of spectral tests to assess the likelihood that a given pixel contains clouds or clear sky. The likelihood is described in terms of clear sky confidence: *confident clear*, *probably clear*, *probably not clear*, and *confident not clear*. The MODIS cloud mask is robust for most cloud types, although thin cirrus with optical depths <0.4 are an exception and are frequently missed [*Ackerman et al.*, 2008; *Cho et al.*, 2008]. The infrared cloud phase [*Platnick et al.*, 2003] is reported at 5 × 5 km resolution and requires the MODIS cloud mask and two MODIS channels, one at 8.5 μm (band 29) and the other at 11 μm (band 31). Clouds are reported as *ice*, *liquid water*, *unknown*, and *mixed phase*. As described by NK08, the *unknown* and *mixed-phase* categories can be considered together as one larger "unknown" category that contains ice, liquid, or a mixture of phases. Several studies have described in detail the strengths and limitations of the MODIS infrared cloud phase mask [NK08; *Cho et al.*, 2008, 2009]. To summarize the results of *Cho et al.* [2009], the C5 MODIS infrared phase algorithm compares well with CALIPSO for opaque high and low clouds, but tends to classify thin cirrus clouds as either water or unknown phase, and classifies the majority of opaque mid-temperature (roughly 250–265 K) clouds as unknown phase. This is because there is not enough spectral phase information in the relatively broad MODIS 8.5 and 11 μm channels to distinguish phase for mid-layer clouds and the thermodynamic phase–cloud temperature relationships assumed by the MODIS algorithm break down for the transparent-cloud cases.

[9] The AIRS instrument is designed to observe atmospheric temperature, water vapor, minor gas species (e.g., H_2O, O_3, N_2O, CH_4, CO, SO_2, and CO_2), clouds, and surface properties [*Chahine et al.*, 2006]. AIRS is an IR grating spectrometer observing the terrestrial thermal IR spectrum from 3.7–15.4 μm while scanning ±48.95° off-nadir at a spectral resolution of $\lambda/\Delta\lambda \sim 1200$ for near daily global coverage. The observational gap from 8.22–8.81 μm makes direct radiance comparisons to MODIS Channel 29 centered at 8.55 μm unfeasible (NK08). The footprint diameter is approximately 13.5 km at nadir expanding to 30 km or greater at high scan angles. The channel noise (NEdT) is well characterized and is on the order of 0.1–0.3 K at 250 K for the channels of interest in this study. Cross-comparisons of AIRS and MODIS T_b in clear sky [*Tobin et al.*, 2006], and in heterogeneous and homogeneous cloud cover [*Schreier et al.*, 2010], show agreement within 0.1–1.0 K for the mid IR channels in the 8–12 μm region.

[10] The AIRS spectrum is rich with an assortment of channels located on gaseous absorption lines, as well as "window channels" in between absorption lines. Window channels are preferable for cloudy remote sensing because absorption line effects that complicate the interpretation of cloudy IR spectra are either minimized or eliminated. To maximize the sensitivity of AIRS to phase discrimination, the approach presented in *Kahn et al.* [2005] and NK08 is used, namely, to maximize the spectral differences in the liquid water and ice indices of refraction while selecting the cleanest window channels possible that have high clear sky transmissivity and low noise over the length of the AIRS mission. Four channels were selected: three minimize the effects of absorption lines and NEdT (857.358, 960.664, and 1231.330 cm^{-1}, abbreviated as 857, 960, and 1231 respectively), and the fourth is centered on a weak water vapor absorption line (1227.709 cm^{-1}, abbreviated as 1227).

[11] The four AIRS channels were combined to form three different ΔT_b that are primarily sensitive to ice cloud particle size ($\Delta T_{960-857}$, abbreviated as ΔT_{si}) [e.g., *Kahn et al.*, 2003], column water vapor ($\Delta T_{1231-1227}$, abbreviated as ΔT_{wv}) [*Aumann et al.*, 2006], and cloud thermodynamic phase ($\Delta T_{1231-960}$, abbreviated as ΔT_{ph}) (NK08). Although the emphasis of this paper quantifies phase sensitivity ΔT_{ph} as a function of cloud state, it is not decoupled from other forms of geophysical variability. For instance, in high altitude transparent and broken clouds or low altitude clouds of any character, variations in the column water vapor (CWV) burden (ΔT_{wv} is useful as a proxy) lead to variations in the magnitude of the emission from the water vapor continuum, which in turn impacts ΔT_{ph}. Similarly, variations in ice

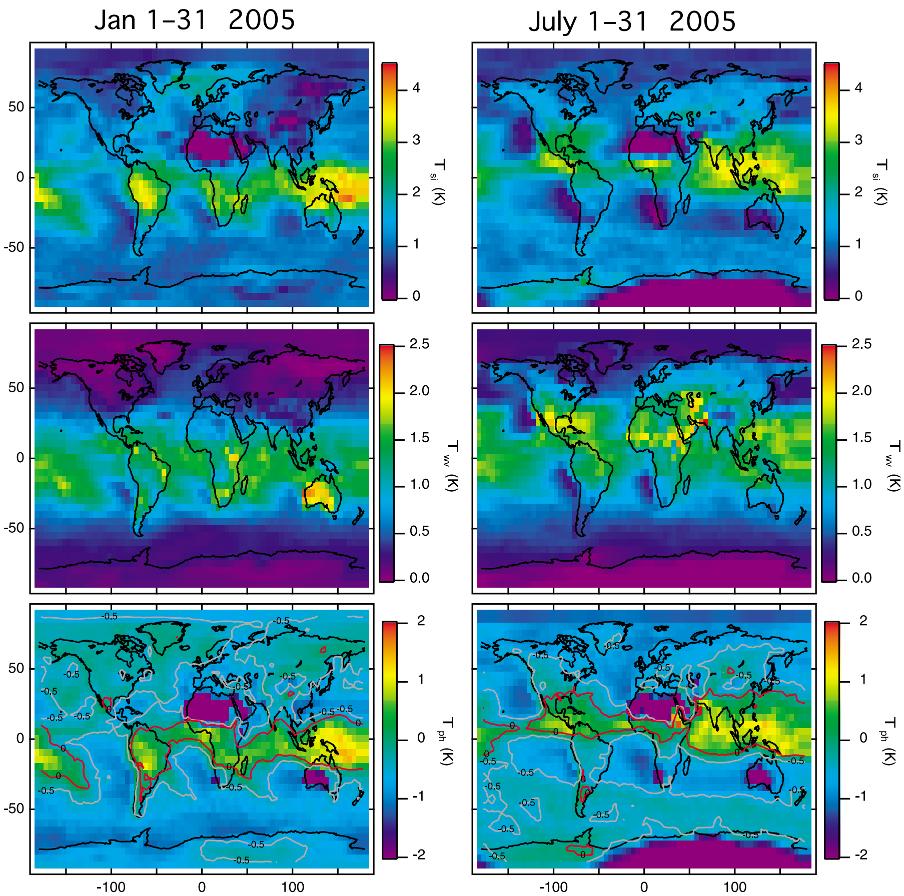

Figure 1. AIRS ΔT_{si}, ΔT_{wv}, and ΔT_{ph} channel differences during (left) January and (right) July 2005. The 0 K and –0.5 K contours are highlighted in red and gray, respectively, in the ΔT_{ph} maps.

cloud particle size (ΔT_{si} is useful as a proxy) can lead to variations in ΔT_{ph} with all else equal. Global maps of the mean values of ΔT_{si}, ΔT_{wv}, and ΔT_{ph} for January and July 2005 are shown in Figure 1. Focusing on ΔT_{si}, observe that the largest values are associated with regions of convection where small particle and semi-transparent ice clouds are most frequent [*Prabhakara et al.*, 1988; *Kahn et al.*, 2008]. The values are reduced at higher latitudes and in regions with stratocumulus clouds, and negative values are found over Antarctica and eastern Siberia during winter (high frequency of thermal inversions) and desert surfaces such as the Sahara and Tibet (strong surface emissivity features). For ΔT_{wv}, the highest values are in the tropics with lower values associated with regions of subsidence in the subtropics and higher latitudes, tracking the well-characterized climatology of CWV [*Randel et al.*, 1996].

[12] Next, ΔT_{ph} shows a more variable pattern than ΔT_{si} and ΔT_{wv}, although the positive differences tend to track thin cirrus in the tropics with an overall lower magnitude than ΔT_{si}. For $\Delta T_{ph} < -0.5$ K, the highest frequencies are found in the stratocumulus and trade cumulus regions in the subtropics and in the mid- and high latitude storm tracks. However, the greatest frequencies of $\Delta T_{ph} < -0.5$ K are concentrated in the summer hemispheres, consistent with climatologically larger frequencies of liquid water clouds, while values of 0.0 K > ΔT_{ph} > −0.5 K are more frequent in the winter hemispheres. The values of −0.5 and 0.0 K approximately correspond to bounds for ice (ΔT_{ph} > 0.0 K) and liquid (ΔT_{ph} < −0.5 K) cloud sensitivity according to idealized near nadir simulations of homogeneous and opaque cloud layers (NK08). Very low values of ΔT_{ph} associated with low surface emissivity at 1231 cm^{-1} are seen over the Saharan, Australian, and Kalahari deserts.

3. Cloud Variability Within the AIRS FOV

[13] Determining the spatial and temporal distribution of cloud heterogeneity within the AIRS FOV is essential for identifying candidate geophysical conditions for improving cloud phase estimates from the passive IR, either by a simple approach using ΔT_{ph} as used in this study, or a more complex algorithm [*Jin et al.*, 2010]. A more refined approach that quantifies cloud uniformity using the variability of MODIS cloud top temperature T_{CLD} will be described in section 5. This is an important distinction because an AIRS FOV completely covered with cloud may contain a wide variety of single and multilayered cloud configurations that could ultimately impact the determination of cloud thermodynamic phase.

[14] Using the collocation methodology of *Schreier et al.* [2010], individual AIRS FOVs are classified as "homogeneous" cloud cover (HOM) when all MODIS

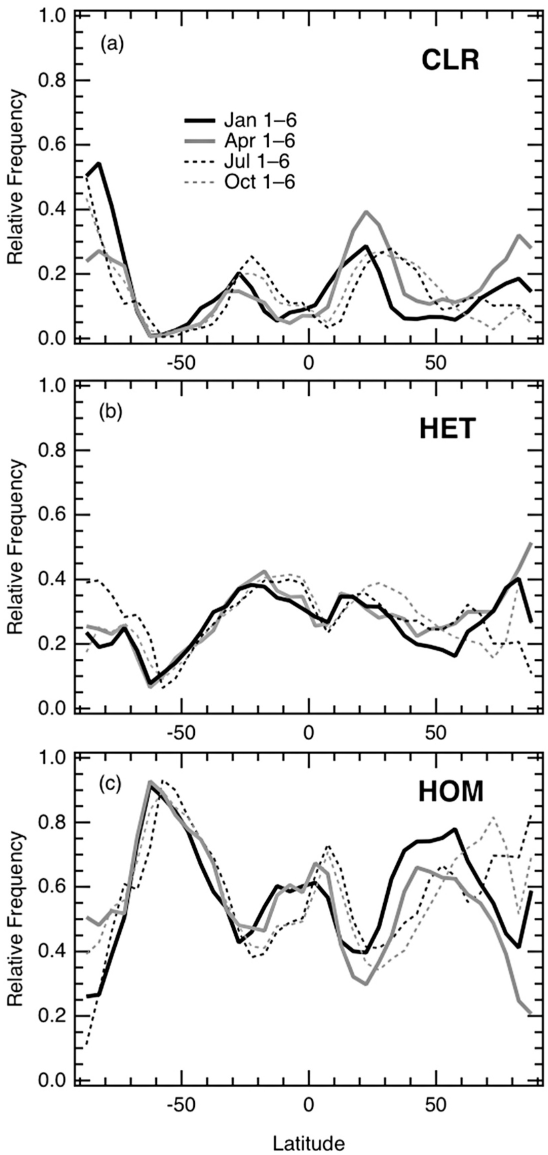

Figure 2. The relative zonal frequencies of (a) clear (CLR), (b) heterogeneous cloud cover (HET), and (c) homogeneous cloud cover (HOM) at the scale of the AIRS footprint for January, April, July, and 1–6 October 2005. Scenes are CLR if all MODIS 1 km cloud mask pixels matched within the AIRS footprint are *confident clear* or *probably clear*. For scenes with HOM, all cloud mask pixels are *confident cloud* or *probably cloud*. For HET, there is a mixture of clear and cloud within the AIRS footprint.

pixels within the AIRS FOV are classified as *probably cloud* or *confident cloud* by the MODIS cloud mask. Scenes fall into our "clear" category (CLR) when the co-located MODIS scenes all are classified as either *probably* or *confident clear* by the cloud mask. The "heterogeneous" cloud cover category (HET) is applied when the co-located MODIS scenes have a mix of clear and cloudy categories. For the time periods in 2005, zonal averages are shown in Figure 2. HOM and CLR have similar distributions as established cloud and clear sky climatologies [e.g., *Rossow and Schiffer*, 1999], while CLR is consistent with expectations of a sensor with AIRS-like spatial resolution [*Krijger et al.*, 2007]. In the case of HET, it is correlated in latitude to CLR with peaks in the subtropics (30–40%) on either side of the ITCZ. Low frequencies of HET (10–25%) are found in the midlatitude storm tracks, especially in the SH. HOM dominates the tropics (50–70%) and the midlatitude storm tracks (60–90%). There is a distinct seasonal migration of CLR and HOM with latitude in the subtropics and high latitudes, and a smaller shift observed with HET. Figure 3 illustrates the horizontal distributions of HOM frequencies shown in Figure 2. As in Figure 1, the highest frequencies of HOM are found in the tropics and storm tracks; however, there are significant differences between the oceans and continents in the tropics and NH, while the distributions are more or less zonally symmetric in the SH.

[15] To address the spatial heterogeneity of clouds in the T_b range of *potentially mixed-phase* (PMP) clouds where contemporary passive techniques cannot differentiate between liquid and ice (e.g., NK08), the samples in Figure 3 are limited to $250 < T_{b,1231} < 265$ K in Figure 4. In the SH storm track region, 30–50% of clouds are simultaneously HOM and within $250 < T_{b,1231} < 265$ K, with a ~10% increase or decrease depending on season. The seasonal differences may be a partial result of the limited sample size (~6 days) for each time period, but may also be caused by seasonal changes in temperature and baroclinic wave activity. However, they are consistent with reduced cloud inhomogeneity observed in the summer with MODIS Level 3 data [*Oreopoulos and Cahalan*, 2005]. A significant drop-off occurs over the Antarctic continent, where fewer clouds are observed. In the NH storm track and Arctic region, the values are highly variable especially between land and ocean, although this behavior may be a partial consequence of the sample size. Note that a wide area of 10–30% frequency is found between 40 and 70°N for all time periods.

[16] Although HOM clouds are better candidates for cloud thermodynamic phase assessment than HET clouds (Figure 5), some HET may exert a large enough spectral signature in ΔT_{ph} to discriminate liquid from ice cloud. However, HET cases within $250 < T_{b,1231} < 265$ K are essentially nonexistent at low and middle latitudes, but the frequencies are as high as 10–20% south of 60°S, and in the Arctic, N. American, and Asian landmasses at lower latitudes during winter (not shown). Later in this study, a nonnegligible proportion of HET will be shown to contain ΔT_{ph} differences large enough to determine the presence of liquid or ice cloud. The land/ocean differences and zonal symmetry seen in HOM are similar for HET, except that there is a strong inverse relationship in frequencies of occurrence. For both time periods, CLR frequencies greater than 30% are only observed over or near major landmasses (Figure 6).

4. Simulations of Clear Sky ΔT_b

[17] The high frequency of HOM at the AIRS FOV-scale in the mid- and high latitudes suggests that AIRS, and other hyperspectral infrared sounders including the Infrared Atmospheric Sounding Interferometer (IASI) and Cross-track Infrared Sounder (CrIS), will be relevant for improved

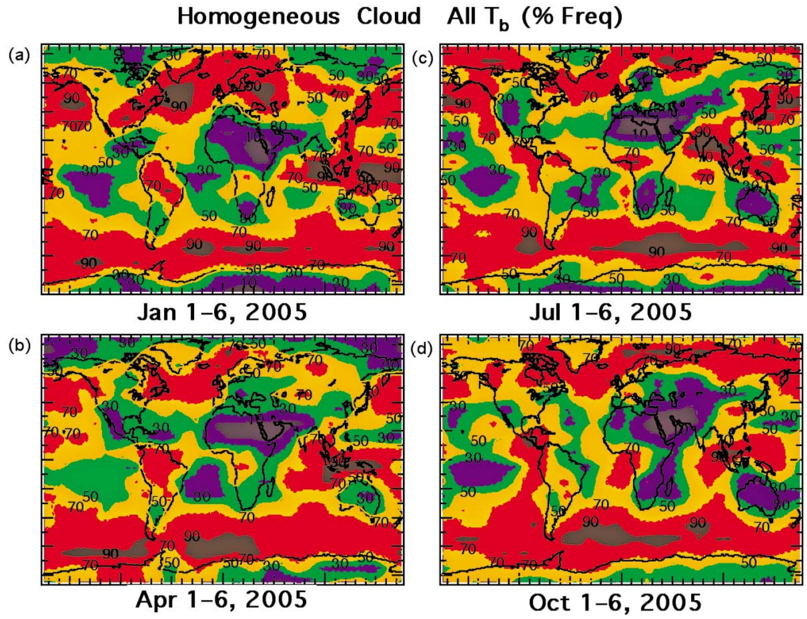

Figure 3. Frequency of all HOM at the AIRS footprint scale for scenes with all values of $T_{b,1231}$. (a) 1–6 January, (b) 1–6 April, (c) 1–6 July, and (d) 1–6 October 2005.

estimates of cloud phase. Idealized radiative transfer simulations (e.g., NK08) demonstrate that AIRS has skill to identify the radiative signature of cloud phase more often than MODIS, even when liquid and ice clouds occur at the same altitude. However, the simulations in NK08 were limited to standard midlatitude winter and summer atmospheres that do not capture the full range of variability of atmospheric CWV. The impacts on ΔT_{ph} will be, to first order, a function of the magnitude of CWV [*Kahn et al.*, 2005] for CLR and HET. In this section, results from a series of radiative transfer calculations of ΔT_{si}, ΔT_{wv}, and ΔT_{ph} for clear sky are presented. These calculations are used to interpret observed differences of ΔT_{si}, ΔT_{wv}, and ΔT_{ph}. The primary objective for simulating ΔT_b is that it is necessary for determining if the signal for cloudy (HET or HOM) ΔT_b is significantly different from that of clear sky conditions.

[18] The radiative transfer simulations are based on a version of the AIRS Stand-Alone Radiative Transfer Algorithm (SARTA) [*Strow et al.*, 2006]. Nadir (7° scan angle) and off-

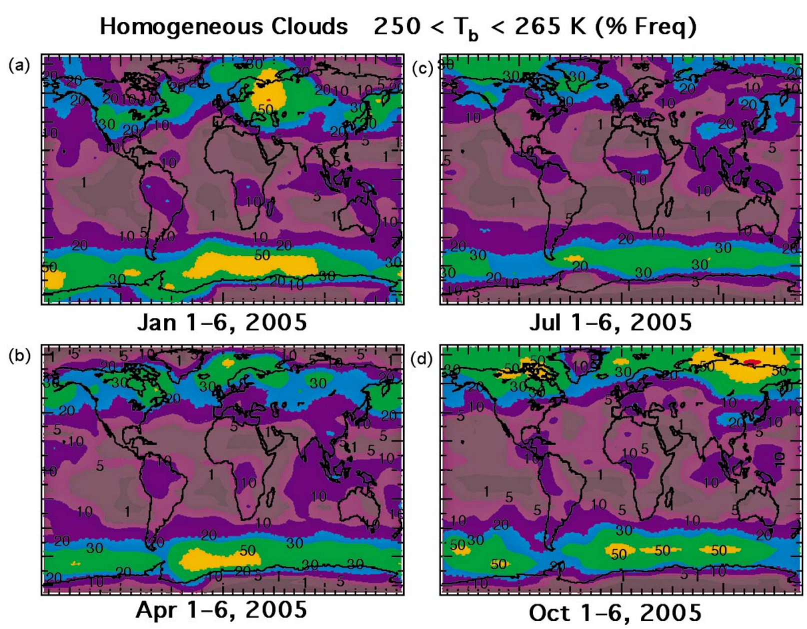

Figure 4. Same as Figure 3 except for HOM clouds restricted to 250 K < $T_{b,1231}$ < 265 K.

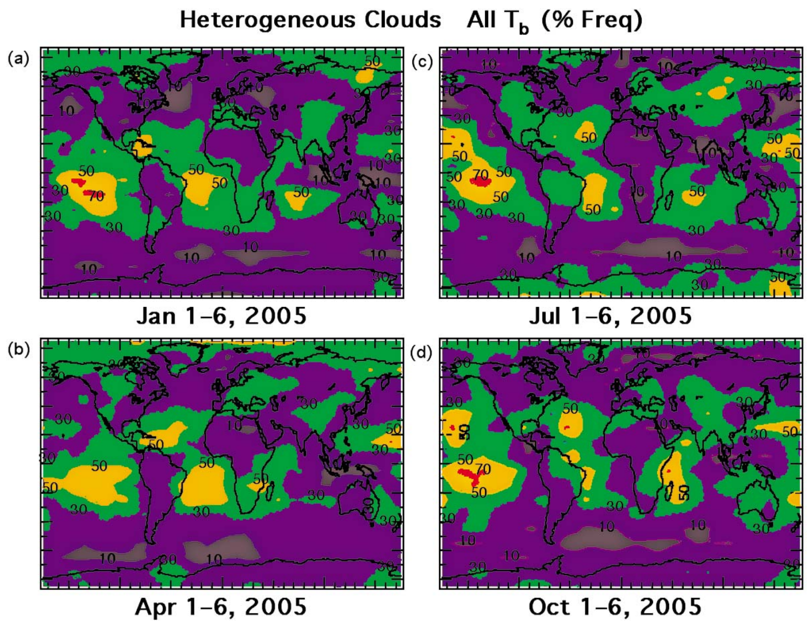

Figure 5. Same as Figures 3 and 4 except for all HET clouds.

nadir (23° and 40° scan angles) simulations were performed for a standard midlatitude summer atmosphere temperature profile in clear skies, while a profile of water vapor was adjusted between 10 and 120% (in increments of 10%) of a base column value (51.4 mm). The surface emissivity (ε) is a composite wave number dependent value obtained from numerous clear-sky AIRS profiles from the subtropical eastern Pacific Ocean. A second set of simulations is shown to demonstrate its sensitivity assuming ε = 0.98 at all wave numbers. The impact of this test depends on the particular ΔT_{b} considered. The magnitude of ΔT_{ph} increases by 0.3 K in the fixed ε case at low CWV, while ΔT_{si} and ΔT_{wv} are less affected because ε in both simulated cases are nearly identical at each channel. When considering potential impacts from different temperature and water vapor profiles, *Kahn et al.* [2005] showed that the dominant source of ΔT_{b} is primarily driven by the magnitude of CWV rather than variability in the vertical structure of temperature and water vapor. The results of these simulations for ΔT_{si}, ΔT_{wv}, and ΔT_{ph} are shown in Figure 7. Even though all three ΔT_{b}s increase as CWV is increased, the relationships between ΔT_{b} and CWV is not necessarily linear nor identical between the different sets of ΔT_{b}s.

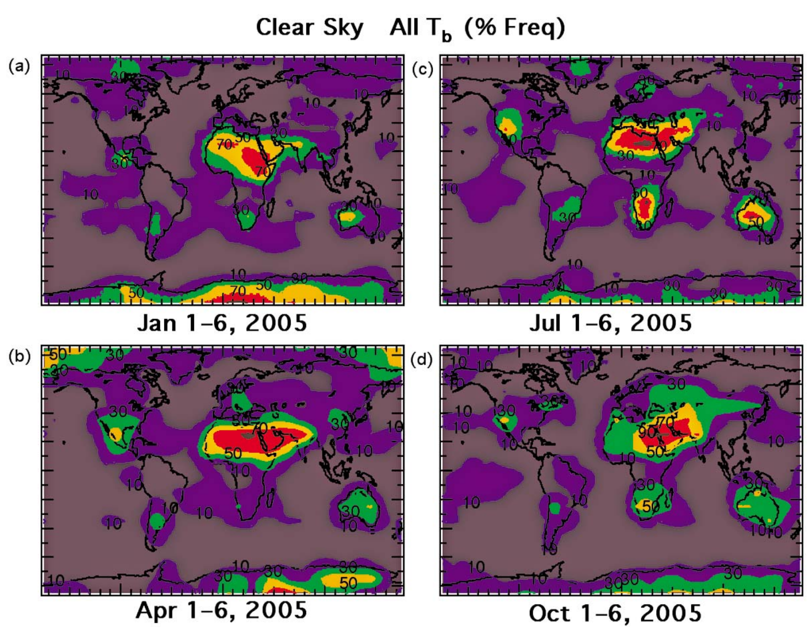

Figure 6. Same as Figures 3–5 except for all CLR.

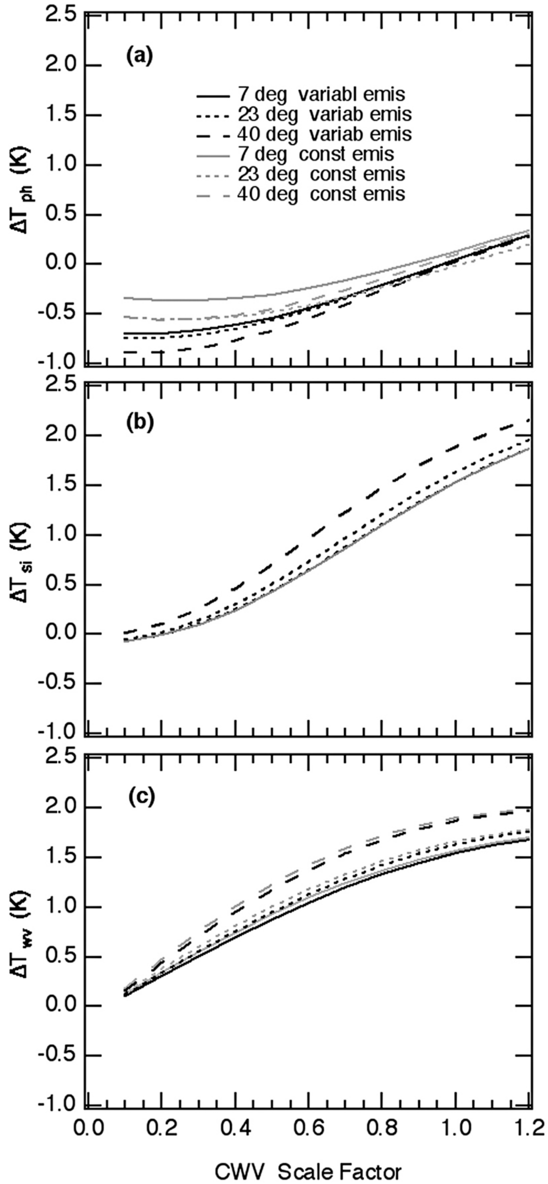

Figure 7. Clear sky ΔT_b for the three channel differences (ΔT_{ph}, ΔT_{si}, and ΔT_{wv}) described in Figure 1. A standard midlatitude profile of temperature was used in the calculation. The CWV is scaled from 10–120% of its original value (51.4 mm) to demonstrate the impacts on ΔT_b. The solid curves are for spectrally varying ε and the gray curves are for a fixed $\varepsilon = 0.98$.

[19] Clear sky "bounds" between pairs of ΔT_b (i.e., ΔT_{si} versus ΔT_{wv}, ΔT_{ph} versus ΔT_{si}, and ΔT_{ph} versus ΔT_{wv}) are simulated at near nadir view using observed values of NEdT for the four channels discussed in section 2 (Figure 8) using the spectrally varying ε. The clear sky bounds depend slightly on scan angle (not shown). A total of 10,000 randomized simulations are performed assuming the channel noise is Gaussian. The 1-σ bounds of the noisy simulations are also shown in Figure 8; these simulations are used in the remainder of this work to highlight the range of ΔT_b that could be explained by clear sky. The noisy clear sky simulations are most compact for the ΔT_{ph} versus ΔT_{wv} histogram compared to the other two-dimensional histograms.

5. Observations of ΔT_b

[20] In this section, we present AIRS observations of the same ΔT_b relationships shown in Figures 7 and 8. As described earlier, we selected three channels that minimize the effects of absorption lines and NEdT (857, 960, and 1231 cm^{-1}), and one centered on a weak water vapor absorption line (1227 cm^{-1}). These channels were combined to form three different ΔT_b that are primarily sensitive to ice cloud particle size (ΔT_{si}, 960–857 cm^{-1}), column water vapor (ΔT_{wv}, 1231–1227 cm^{-1}), and cloud thermodynamic phase (ΔT_{ph}, 1231–960 cm^{-1}). Each two-dimensional histogram and its relevance are described in detail below.

5.1. ΔT_{si} Versus ΔT_{wv} and ΔT_{ph} Versus ΔT_{si}

[21] Three different two-dimensional histograms of AIRS, ΔT_{si} versus ΔT_{wv}, ΔT_{ph} versus ΔT_{si}, and ΔT_{ph} versus ΔT_{wv} for all sky conditions (1–6 January 2005) are shown in Figure 9 for three sets of AIRS scan angles (±15° within nadir, ±15–30°, and > ± 30°). The ΔT_{ph} versus ΔT_{si} histogram (middle row) shows that a large majority of observed values have $\Delta T_{ph} < 0$ K and $\Delta T_{si} > 0$ K (Figure 9). There is a notable area of scatter that is skewed toward positive values of ΔT_{ph} and even larger positive values of ΔT_{si} that are associated with cirrus clouds. The scatter associated with these cirrus clouds are truncated in these diagrams. The peak frequency of occurrence resides within the simulated bounds of clear sky. However, a significant portion of the observations is located outside of the clear sky bounds. HET clouds dominate the points within the clear sky bounds (not shown), while a majority of HOM clouds reside outside of the clear sky bounds (not shown). Similarly, for ΔT_{si} versus ΔT_{wv} (top row), most values of ΔT_{si} and ΔT_{wv} are positive, but two distinct modes of scatter are observed. The first is associated with $\Delta T_{wv} < 0.5$ K while the second is associated with positive increases in both ΔT_{si} and ΔT_{wv}. The first mode is dominated by HOM cloud (not shown) while the second is dominated by HET cloud (not shown). This is entirely consistent with an increasing magnitude of ΔT_{wv} in the presence of broken cloud cover, where higher values of CWV increase ΔT_{wv}, especially in the tropics [*Aumann et al.*, 2006]. In opaque cloud cover or in regions with low CWV, the magnitude of ΔT_{wv} remains minimal.

5.2. ΔT_{ph} Versus ΔT_{wv}

[22] The previous two-dimensional histograms (top and middle rows of Figure 9) reveal that the most frequent observational occurrences of ΔT_b are found within the simulated bounds of clear sky. This is not the case with ΔT_{ph} versus ΔT_{wv} as a large majority of points are located outside of the clear sky bounds (bottom row Figure 9). Since the instrument noise for 857 cm^{-1} is 3–4 times larger than that of the other channels, ΔT_{si} offers a less useful constraint on phase detection compared to ΔT_{wv}. Figure 8 shows a broader area of scatter associated with clear sky ΔT_{si} because of higher noise at 857 cm^{-1}. This implies that isolating geophysical variability (e.g., cloud thermodynamic phase) is more challenging when using ΔT_{si}. For a particular AIRS FOV, it is possible that ΔT_{si} may be able to discriminate between

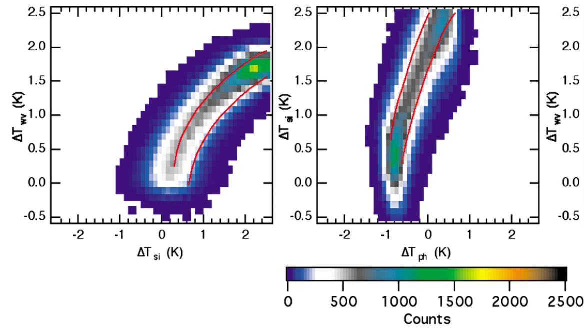

Figure 8. Simulated clear sky PDFs of (a) ΔT_{si} versus ΔT_{wv}, (b) ΔT_{ph} versus ΔT_{si}, and (c) ΔT_{ph} versus ΔT_{wv} for the spectrally varying ε case of Figure 7 for near nadir view.

liquid and ice phases when other ΔT_bs cannot. For practical purposes, multiple tests could be implemented in a retrieval of cloud thermodynamic phase [e.g., *Jin et al.*, 2010]. However, these results suggest this channel difference is less relevant compared to ΔT_{ph} and ΔT_{wv}. Additionally, channel noise is an important consideration for phase assessment, and composites of several channels with nearly identical weighting functions should be formed to obtain further reductions in channel noise. Furthermore, ΔT_{si} is not strongly correlated with cloud heterogeneity, unlike ΔT_{wv}, which is correlated to cloud fraction within a given AIRS FOV. Clouds located in altitude above maximum values of water vapor near the surface can obscure larger values of ΔT_{wv} that arise when CWV is elevated and the sky is otherwise clear.

[23] In the remainder of this paper, the focus is on the ΔT_{ph} versus ΔT_{wv} histogram (Figure 9, bottom row). For

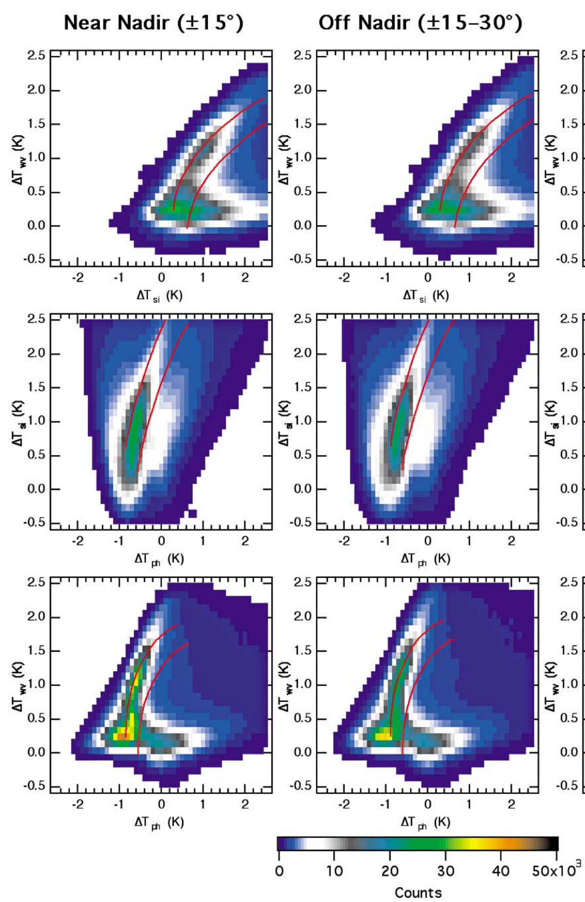

Figure 9. Global AIRS observations of all sky PDFs (1–6 January 2005) for (top) ΔT_{si} versus ΔT_{wv}, (middle) ΔT_{ph} versus ΔT_{si}, and (bottom) ΔT_{ph} versus ΔT_{wv}. All observations are sorted into three AIRS scan angle ranges: ±15° within nadir, ±15–30°, and greater than ±30°. The simulated 1-σ clear sky bounds from Figure 8 are also shown with red lines. The all sky PDFs for the other time periods are similar and are not shown for sake of brevity.

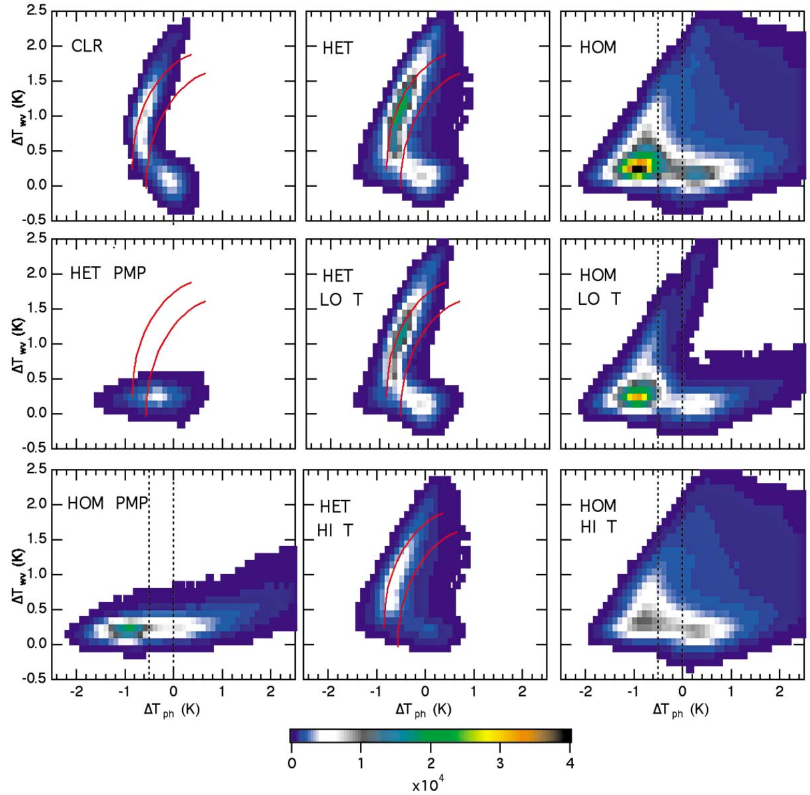

Figure 10. The ΔT_{ph} versus ΔT_{wv} histograms for the near nadir observations (1–6 January 2005). The top row is for CLR, HET, and HOM cloud cover. The other panels show observations for HET and HOM for 250 K < $T^{-1}_{b,\ 1231\ cm}$ < 265 K, and both HET and HOM for clouds with high σ_T (labeled as HI T) and low σ_T (labeled as LO T). The red lines approximate the 1-σ envelope of clear sky observations, while the vertical black lines approximate the phase sensitivity in NK08. The color scale for the counts in each panel is identical.

ΔT_{ph} versus ΔT_{wv}, a complex picture of ΔT_b scatter is revealed. At near nadir view, there is one distinct frequency maximum centered near a value of $\Delta T_{ph} = -0.8$ to -1.0 K, and a less distinct mode near +0.2 K. The mode at $\Delta T_{ph} = -0.8$ to -1.0 K extends toward higher ΔT_{wv} and curves toward $\Delta T_{ph} = 0$ K when ΔT_{wv} is about +2.0 K. For the off-nadir angles, the negative ΔT_{ph} mode shifts toward increasingly negative values, whereas this does not occur for the mode near 0 K.

[24] These distinct modes are revealed in more detail in Figure 10 for near nadir observations. The two-dimensional histogram in Figure 9 (bottom row, left) is partitioned into CLR, HET, and HOM portions for all values of $T_{b,1231}$ (top row), cases with significant cloud layer uniformity with the standard deviation of T_{CLD} (σ_T) < 2 K, and reduced cloud uniformity with $\sigma_T \geq 2$ K. Subsets for $T_{b,1231}$ between 250 and 265 K are also shown (left column). As before, the 1-σ simulated bounds of clear sky are superimposed on top of the observed ΔT_b for CLR and HET, while the phase delineation in NK08 is shown as vertical lines for HOM (Figure 8). A majority of cases (59.5%) are identified as HOM (Table 1). The two modes identified above for small

Table 1. Shown is the Global Relative Frequency of All Scene Types for 1–6 January and 1–6 July 2005[a]

Type of Sky	$T_{b,1231}$	1–6 January 2005	1–6 July 2005
Clear	*All*	*14.2%*	*13.1%*
Het Cld	*All*	*26.3%*	*28.0%*
Het Cld	250–265 K	3.5%	1.5%
Hom Cld	*All*	*59.5%*	*58.9%*
Hom Cld	250–265 K	17.6%	12.8%
Hom Ice Cld	All	10.3%	10.7%
Het Liquid Cld	All	14.8%	17.1%
Hom Liquid Cld	All	16.3%	18.5%
Hom Unknown + Mixed Phase Cld	All	6.2%	3.5%

[a]The italicized first, second, and fourth rows (CLR, HET, and HOM) sum to 100% following Figure 2. Several other categories are shown that restrict observations from 250 to 265 K and the scene type is based on the MODIS infrared cloud phase mask (ice, liquid, and unknown + mixed phase).

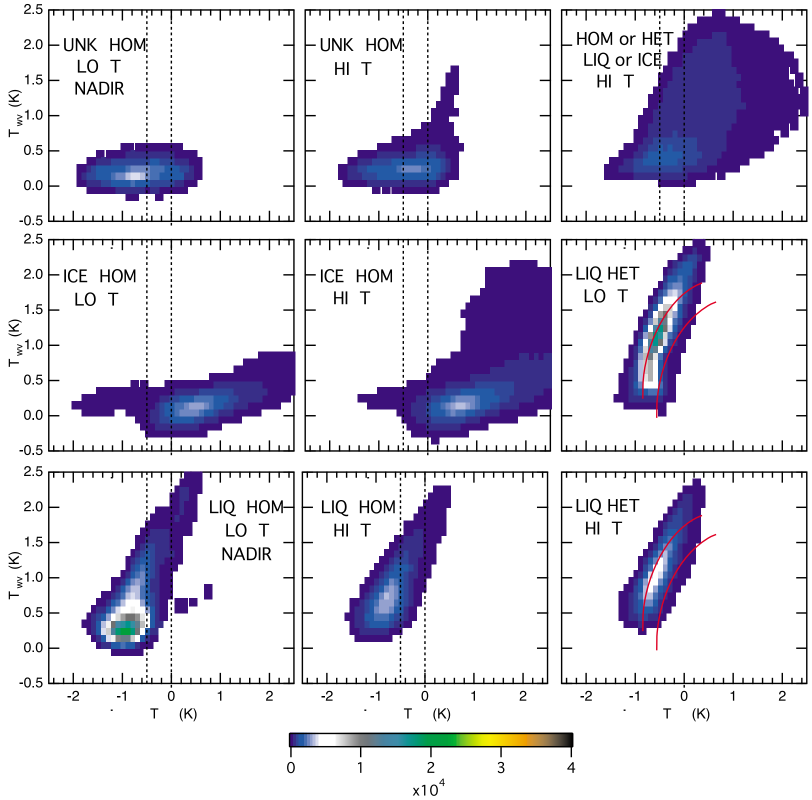

Figure 11. Similar to Figure 10 except the cloud categories are further subdivided by MODIS cloud thermodynamic phase. Shown are UNK HOM, ICE HOM, LIQ HOM, and LIQ HET with high or low σ_T. One additional "mixed" category is included, which contains either HET or HOM clouds containing mixtures of LIQ and ICE ($\sigma_T \geq 2$ K only).

values of ΔT_{wv} separate more clearly in the HOM case than for all sky conditions in Figure 9. The portion of the first mode with higher values of ΔT_{wv} is mostly associated with HET, although a similar pattern is observed in CLR as well. For HET and CLR, the mode that appears near 0 K for both ΔT_{wv} and ΔT_{ph} is associated with cold surfaces at high latitudes. The mode in the HET and CLR cases with $\Delta T_{wv} >$ 0 K and $\Delta T_{ph} < 0$ K is primarily located over lower latitude oceanic regions within the trade wind cumulus regime. Furthermore, the scatter toward positive values of ΔT_{wv} is less pronounced in CLR compared to HET, consistent with drier air in clear regions that dominate the subtropics. Finally, significant differences are found between more uniform ($\sigma_T < 2$ K) and less uniform ($\sigma_T \geq 2$ K) clouds. The phase separation is much more pronounced for clouds with $\sigma_T <$ 2 K compared to those with $\sigma_T \geq 2$ K.

[25] Note that in both the CLR and HET cases, the peak frequency tends to occur toward more negative values of ΔT_{ph} rather than centered between the two clear sky bounds. This suggests that (1) the clear sky simulations may not represent the full range of clear sky ΔT_b observed in nature, (2) we are seeing the effects of undetected cloud in the MODIS *probably clear* and *confident clear* categories, and (3) the classification of cloud phase in HET footprints with AIRS radiances could be challenging because of close similarities to CLR. However, the scatter in HET is significantly broader than CLR, suggesting that some proportion of HET is classifiable as either ice or liquid phase. Given that a higher proportion of scatter is to the negative side of ΔT_{ph} and is spatially correlated to trade cumulus over the oceans (not shown), most cases of HET are probably liquid phase. For challenging cases of HOM when $T_{b,1231}$ is between 250 and 265 K, very good separation is found between likely cases of liquid and ice clouds, with the vast majority as liquid phase. For CLR and HET, the frequencies are far fewer than HOM (Table 1).

5.3. ΔT_{ph} versus ΔT_{wv} Conditioned by Cloud Phase, Effective Cloud Fraction, and Column Water Vapor

[26] To assess the potential overlap in phase identification between AIRS and MODIS, the infrared cloud phase from MODIS is mapped to the ΔT_{ph} versus ΔT_{wv} histogram for the near nadir view (Figure 11) with both high ($\sigma_T < 2$ K) and low ($\sigma_T \geq 2$ K) cloud uniformity. The nine panels in Figure 11 are partitioned by single-phase classifications of ice, liquid, and unknown + mixed phase within the AIRS FOV and one category containing a mixture of LIQ and ICE. The most frequent type is LIQ HOM cloud with $\sigma_T <$ 2 K, consistent with the MODIS phase climatology (NK08). A vast majority of these cases have $\Delta T_{ph} < -0.5$ K, demonstrating that AIRS phase estimates are likely to be consistent with MODIS-detected LIQ HOM clouds. The tail of scatter extending toward larger values of ΔT_{wv} and ΔT_{ph} is consistent with transparent HOM (or low altitude HOM with a large portion of CWV above cloud top) that allows the radiative signature of water vapor to be observed. For LIQ

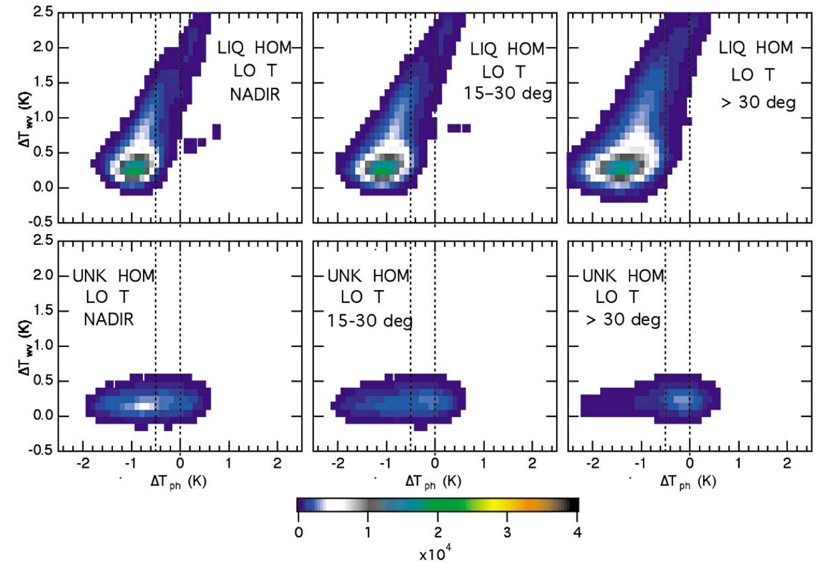

Figure 12. (top) LIQ HOM and (bottom) UNK HOM for clouds with high σ_T for the three groups of scan angles (±15° of nadir, ±15–30°, and > ± 30°).

HOM clouds with $\sigma_T \geq 2$ K, these cases are less frequent and contain a smaller ΔT_{ph} difference. For LIQ HET clouds, they behave in a similar manner as all types of HET clouds (Figure 10) and little difference between the two categories of cloud uniformity is observed. However, a significant population of the scatter is to the left of the clear sky 1-σ bounds. In the presence of broken liquid clouds such as trade cumulus, which frequently have cloud fractions <20–30% [e.g., *Medeiros et al.*, 2008], the ΔT_b resembles a spectral signature somewhere in between that of uniform liquid water cloud and clear sky, perhaps closer to the latter than the former given their expected range of cloud fraction. Furthermore, a small proportion of MODIS-identified liquid clouds may be misclassified [*Cho et al.*, 2009]. Clearly, HET clouds are a substantial challenge for phase identification, but most occur in the subtropics and tropics and are easily classified as liquid by other means, such as T_{CLD}.

[27] With regard to HOM unknown + mixed phase (UNK) clouds, the peak frequency of ΔT_{ph} is centered within the bounds of phase uncertainty described in NK08 for $\sigma_T \geq 2$ K, but is outside of the bounds for $\sigma_T < 2$ K. This suggests that in more uniform "uncertain" clouds, AIRS may be able to more easily infer that these clouds are liquid phase. Next, HOM ice clouds (according to MODIS) are shown in Figure 11. The vast majority have $\Delta T_{ph} > 0$ K, although a small number have values of $\Delta T_{ph} < 0$ K. These kinds of misclassifications are consistent with multilayer clouds containing overlapping ice above liquid layers. There is little difference between HOM ice clouds with $\sigma_T \geq 2$ K and $\sigma_T < 2$ K, indicating that cloud uniformity does not greatly impact ice phase discrimination. Also note that a mixture of ICE and LIQ for either HET or HOM clouds is shown for $\sigma_T \geq 2$ K and, surprisingly, occurs fairly infrequently. There are virtually no counts for cases with $\sigma_T <$ 2 K (not shown). This mixed category does show that many outliers may be dominated by ICE or LIQ spectral signatures, but the largest number of cases reside approximately within the clear sky bounds of NK08. Since these mixtures are dominated by low values of cloud uniformity ($\sigma_T \geq 2$ K), this suggests at the AIRS FOV scale that LIQ and ICE are frequently located within different vertical layers and very rarely is LIQ and ICE observed in the same layer.

[28] The scan angle dependence of LIQ HOM clouds and unknown + mixed phase HOM uniform clouds ($\sigma_T < 2$ K) are shown in Figure 12. Unlike the UNK clouds that contain liquid-like ΔT_{ph} signatures more often at nadir compared to off-nadir, LIQ have increasingly negative values of ΔT_{ph} with scan angle. This result suggests that cloud thermodynamic phase determination may depend on scan angle in a different manner for each type of cloud. An operational phase algorithm should take scan angle into account.

[29] Zonal averages of the cloud categories presented in the previous figures are shown in Figure 13 separately for the four time periods in 2005. The HOM UNK category in Figure 13 is as high as 5–15% of the overall frequency of total cloud amount in the high latitudes. About half of these cases are probably LIQ or ICE according to AIRS (Figure 11), demonstrating that AIRS will contribute to improvements in cloud phase assessment in the poorly characterized high latitudes. This may also be true of HET clouds with mixtures of UNK, LIQ, and ICE (not shown). A more detailed examination of the effects of phase mixtures on ΔT_{ph} warrants further investigation. Both the HOM and HET liquid categories similarly track the HOM and HET for all cloud types (Figure 2). However, the sharp peak observed in the high latitude SH for HOM in Figure 2 is contained in HOM PMP, not in HOM LIQ, in Figure 13.

[30] Cloud coverage and cloud opacity simultaneously impact the ΔT_{ph} versus ΔT_{wv} histogram. To quantify this simultaneous effect, the ΔT_{ph} versus ΔT_{wv} relationships are sorted into four bins of AIRS effective cloud fraction (ECF [see *Kahn et al.*, 2007]) in Figure 14 for all scan angles: ECF < 0.1, 0.1 ≤ ECF < 0.5, 0.5 ≤ ECF < 0.9, and ECF >

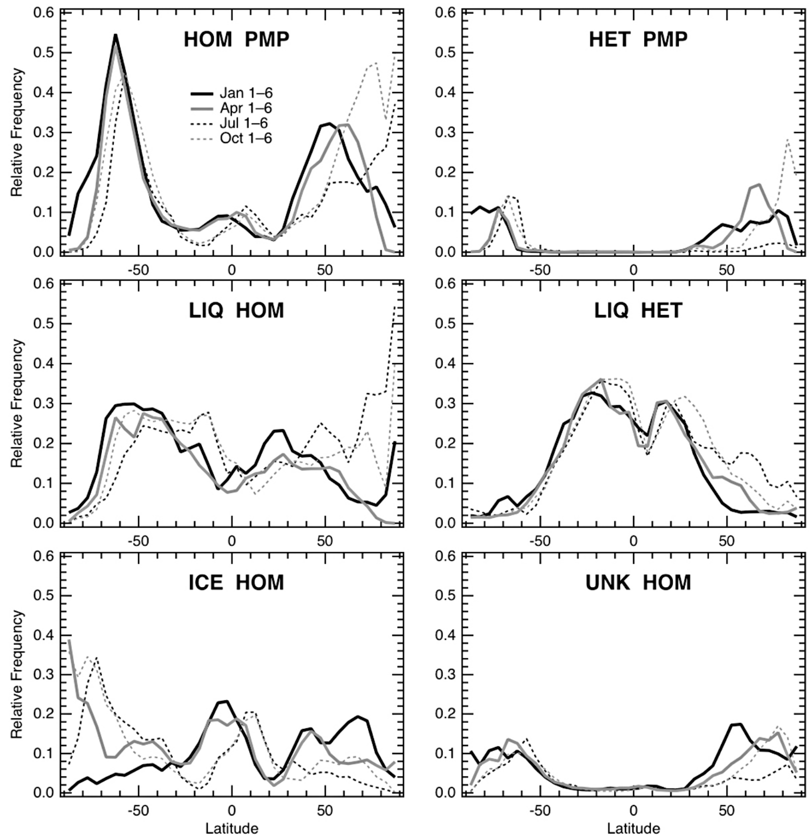

Figure 13. Similar to Figure 2, except several subcategories of cloud are shown. Both HET and HOM clouds for $T_{b,1231}$ between 250 and 265 K (HET PMP and HOM PMP, respectively), HOM ICE, HOM LIQ, HET LIQ, and HOM UNK are shown for all four time periods in 2005.

0.9. The AIRS ECF is a convolution of both cloud coverage and emissivity, unlike the MODIS cloud mask, which represents coverage only. For thin and/or broken cloud cover (ECF < 0.1), most values are near $\Delta T_{ph} = -0.8$ K, with an elongated mode extending toward more positive values of ΔT_{ph} and ΔT_{wv} similar to CLR in Figure 10. However, there is more scatter extending in all directions that is consistent with thin and broken clouds with radiance signatures consistent to liquid or ice phase. Similarly, for higher values of ECF, this scatter increases and the mode consistent with CLR in Figure 10 is further reduced in magnitude. For ECF > 0.5 in Figure 14, the scatter organizes into two distinct modes centered near $\Delta T_{ph} = -0.8$ K and +0.2 K that closely resemble HOM in Figure 10. Lower values of ΔT_{wv} are found for ECF > 0.9 in Figure 14 compared to HOM in Figure 10. This shows that some clouds, although uniformly overcast, may be semi-transparent for HOM in Figure 10, causing an increase of ΔT_{wv}; similar values are found in Figure 14 when $0.5 \leq$ ECF < 0.9. These results are also consistent with an increased sensitivity to cloud thermodynamic phase in the presence of homogeneous and opaque clouds (high ECF) when compared to heterogeneous clouds (low ECF).

[31] To quantify the relationships of CWV to the ΔT_{ph} versus ΔT_{wv} histogram, Figure 14 (ECF < 0.1), repeated in Figure 15, is partitioned into four bins of CWV (CWV < 10 mm, 10 mm < CWV < 30 mm, 30 mm < CWV < 50 mm, and CWV > 50 mm) and one bin for failed retrievals of AIRS/AMSU CWV that are common in precipitating clouds [*Kahn et al.*, 2007]. Low values of ECF that are simply retrieval artifacts are also observed within failed temperature and water vapor retrievals [*Kahn et al.*, 2007]. As expected, the mode centered near $\Delta T_{ph} = -0.8$ K occurs for values of CWV <30 mm. Similarly, the mode with increasing values of ΔT_{ph} and ΔT_{wv} is associated with higher values of CWV. If the bins of CWV are restricted to narrower ranges, the scatter within each bin in the direction of ΔT_{wv} is significantly reduced (not shown). This is consistent with a strong observed correlation between CWV and ΔT_{wv} in AIRS observations [*Aumann et al.*, 2006]. Other bins of ECF (not shown) also reveal a similar behavior, although the higher values of ΔT_{wv} are reduced with increasing values of ECF.

6. Discussion and Conclusions

[32] A combination of spatially collocated Atmospheric Infrared Sounder (AIRS [*Aumann et al.*, 2003]) radiances and Moderate Resolution Imaging Spectroradiometer (MODIS [*Platnick et al.*, 2003]) cloud products are used to quantify the impact of cloud heterogeneity on AIRS-based assessments of cloud thermodynamic phase. The smeared, rotated, and truncated AIRS spatial response functions obtained from prelaunch calibration are used to spatially co-locate radiances and geophysical parameters from AIRS and MODIS [*Schreier*

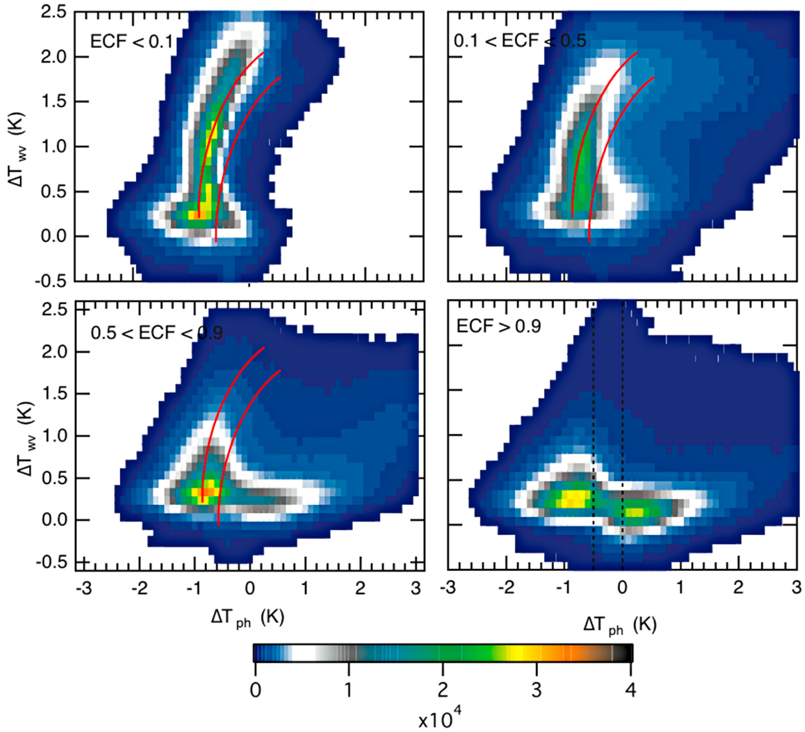

Figure 14. Shown are ΔT_{ph} versus ΔT_{wv} histograms sorted by 4 categories of ECF: (a) 0.0–0.1, (b) 0.1–0.5, (c) 0.5–0.9, and (d) 0.9–1.0 for 1–6 January 2005. No scan angle discrimination is made for ECF. The red lines approximate the 1-σ envelope of clear sky simulations for 23° off nadir, while the vertical black lines approximate the phase sensitivity in NK08.

et al., 2010]. Radiative transfer simulations have demonstrated that AIRS channels (in principle) have greater sensitivity to cloud thermodynamic phase when compared to MODIS channels in similar spectral bands [*Nasiri and Kahn*, 2008]. However, the relative trade-offs of spectral and spatial resolution differences that are inherent between AIRS and MODIS have not been quantified to date. In this investigation, the relative heterogeneity of cloud cover within different cloud and regime types for four time periods (1–6 January, 1–6 April, 1–6 July, and 1–6 October 2005) is

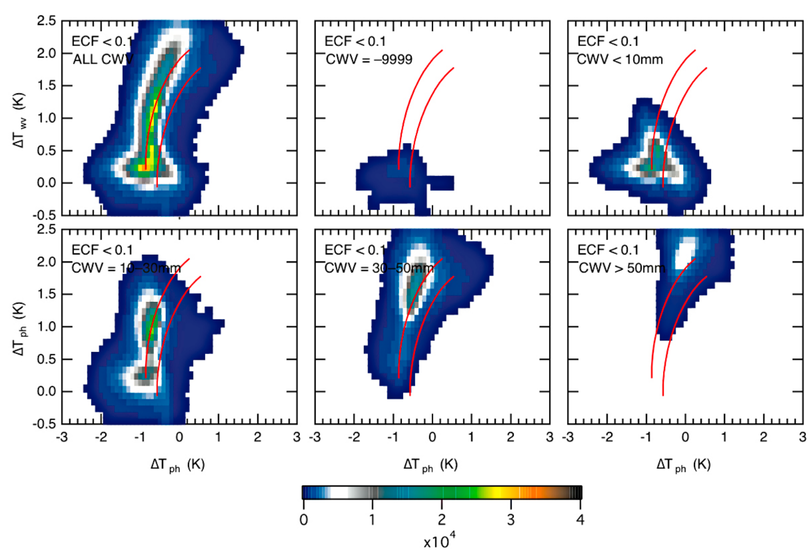

Figure 15. Shown are ΔT_{ph} versus ΔT_{wv} histograms for (a) ECF = 0.0–0.1, sorting CWV from (c) 0–10, (d) 10–30, (e) 30–50, and (f) greater than 50 mm; (b) failed AIRS/AMSU retrievals. The red lines approximate the 1-σ envelope of clear sky simulations for 23° off nadir.

globally quantified and related to the potential of AIRS to improve infrared-based estimates of cloud thermodynamic phase.

[33] The rigorous pixel-scale collocation methodology facilitates a quantitative and rigorous estimate of scene type within a given AIRS field of view (FOV). The MODIS cloud mask [*Frey et al.*, 2008], infrared-based cloud thermodynamic phase [*Platnick et al.*, 2003], and cloud top temperature (T_{CLD}) [*Menzel et al.*, 2008] are used to characterize cloud structure within the AIRS FOV. Global distributions of AIRS FOV-scale frequencies of clear sky (cloud mask *probably* or *confident clear*), homogeneous cloud cover (*probably* or *confident cloud*), and heterogeneous cloud cover (cloud and clear) for a four week time period are found to be 13–14%, 59–60%, and 26–28%, respectively, depending on the time period of study. Homogeneous cloud cover occurs 70–90% of the time in the mid- and high latitude storm track regions, and 30–50% of the time when brightness temperatures (T_b) are between 250 and 265 K. Estimates of the spatial uniformity of T_{CLD} within the AIRS FOV are used as a further quantification of cloud uniformity. The high latitudes have a poor characterization of cloud thermodynamic phase and also show strong responses in forced CO_2 climate change modeling experiments such as changes in cloud altitude, cloud water content, and the poleward migration of clouds [e.g., *Li and Le Treut*, 1992; *Senior and Mitchell*, 1993]. Recent results obtained from the Cloud-Aerosol Lidar with Orthogonal Polarization (CALIOP [*Hu et al.*, 2010]) indicate many of these clouds are liquid phase, while MODIS identifies a majority of these clouds as either "unknown" or "mixed-phase." Since cloud cover is overwhelmingly homogeneous and clouds are more uniform at the AIRS FOV scale in these critical geophysical regimes, AIRS and other hyper-spectral sounders including IASI and CrIS will play a key role toward establishing a global "best estimate" of cloud thermodynamic phase.

[34] Four AIRS channels with low NEdT in between absorption lines with sensitivity to thermodynamic phase and small-scale cloud heterogeneity were identified with approximate wave numbers of 857, 960, 1227, and 1231 cm^{-1}. They are combined to form three different ΔT_b that are primarily sensitive to ice cloud particle size (960–857 cm^{-1}, ΔT_{si}), column water vapor (1231–1227 cm^{-1}, ΔT_{wv}), and cloud thermodynamic phase (1231–960 cm^{-1}, ΔT_{ph}). Both ΔT_{ph} and ΔT_{wv} are shown to be better correlated to cloud heterogeneity and cloud thermodynamic phase than ΔT_{si}. Thus, the focus of this work is on two-dimensional histograms of ΔT_{ph} versus ΔT_{wv}. Homogeneous cloud cover scenes with T_b between 250 and 265 K have substantially larger phase radiance signatures than heterogeneous cloud cover. Furthermore, clouds that are uniform (lower T_{CLD} variability) show even better cloud thermodynamic phase separation than those with higher T_{CLD} variability. A major portion of heterogeneous cloud cover falls within simulated bounds of clear sky of ΔT_{ph}, although a minority of the clouds exert a radiative signature probably large enough to be identified as liquid or ice. Two-dimensional histograms of ΔT_{ph} versus ΔT_{wv} sorted by MODIS cloud thermodynamic phase suggest that approximately 50% of homogenous "unknown + mixed phase" clouds could be identified as liquid or ice with AIRS. At near nadir view angles with low T_{CLD} variability, a majority of clouds appears to be liquid phase. At off-nadir view angles with high T_{CLD} variability the frequencies of liquid and ice phase clouds are more or less similar. A disproportionate number of these clouds are located in the mid- and high latitude storm tracks.

[35] The results of this investigation suggest a new quantitative approach that leverages a combination of existing hyperspectral sounders (e.g., AIRS) with high-spatial-resolution imagers (e.g., MODIS) and their derived geophysical products, to improve infrared-based assessments of cloud thermodynamic phase for a small but important subset of clouds that plays a key role in cloud-climate feedback. This investigation also lays the groundwork for similar observations to be obtained from VIIRS and CrIS on the Joint Polar Satellite Platforms (JPSS) [*Lee et al.*, 2010]. Similarly, this approach is potentially applicable to the characterization of other types of cloud and aerosol parameters, along with temperature and water vapor profiles, and minor gases that are present within complicated scene heterogeneity.

[36] **Acknowledgments.** The authors gratefully acknowledge the constructive feedback of the anonymous reviewers. Funding for BHK and MMS was provided in part by NASA award NNX08AI09G and the AIRS project at the Jet Propulsion Laboratory (JPL). AIRS and MODIS data were obtained through the Goddard Earth Sciences Data and Information Services Center (http://daac.gsfc.nasa.gov). A portion of this work was performed within the Joint Institute for Regional Earth System Science and Engineering (JIFRESSE) of the University of California, Los Angeles (UCLA) and at the Jet Propulsion Laboratory, California Institute of Technology, under contract with NASA.

References

Ackerman, S. A., R. E. Holz, R. Frey, E. W. Eloranta, B. C. Maddux, and M. McGill (2008), Cloud detection with MODIS. Part II: Validation, *J. Atmos. Oceanic Technol.*, *25*, 1073–1086, doi:10.1175/2007JTECHA1053.1.

Aumann, H. H., et al. (2003), AIRS/AMSU/HSB on the Aqua mission: Design, science objectives, data products, and processing systems, *IEEE Trans. Geosci. Remote Sens.*, *41*, 253–264, doi:10.1109/TGRS.2002.808356.

Aumann, H. H., S. Broberg, D. Elliott, S. Gaiser, and D. Gregorich (2006), Three years of Atmospheric Infrared Sounder radiometric calibration validation using sea surface temperatures, *J. Geophys. Res.*, *111*, D16S90, doi:10.1029/2005JD006822.

Barnes, W. L., T. S. Pagano, and V. V. Salomonson (1998), Prelaunch characteristics of the Moderate Resolution Imaging Spectroradiometer (MODIS) on EOS-AM1, *IEEE Trans. Geosci. Remote Sens.*, *36*, 1088–1100, doi:10.1109/36.700993.

Baum, B. A., P. F. Soulen, K. I. Strabala, M. D. King, S. A. Ackerman, W. P. Menzel, and P. Yang (2000), Remote sensing of cloud properties using MODIS Airborne Simulator imagery during SUCCESS 2. Cloud thermodynamic phase, *J. Geophys. Res.*, *105*, 11,781–11,792, doi:10.1029/1999JD901090.

Bony, S., and J. L. Dufresne (2005), Marine boundary layer clouds at the heart of tropical cloud feedback uncertainties in climate models, *Geophys. Res. Lett.*, *32*, L20806, doi:10.1029/2005GL023851.

Cahalan, R. F., W. Ridgway, W. J. Wiscombe, and T. L. Bell (1994), The albedo of fractal stratocumulus clouds, *J. Atmos. Sci.*, *51*, 2434–2455, doi:10.1175/1520-0469(1994)051<2434:TAOFSC>2.0.CO;2.

Chahine, M. T., et al. (2006), AIRS: Improving weather forecasting and providing new data on greenhouse gases, *Bull. Am. Meteorol. Soc*, *87*, 911–926, doi:10.1175/BAMS-87-7-911.

Cho, H.-M., P. Yang, G. W. Kattawar, S. L. Nasiri, Y. Hu, P. Minnis, C. Trepte, and D. Winker (2008), Depolarization ratio and attenuated backscatter for nine cloud types: Analyses based on collocated CALIPSO lidar and MODIS measurements, *Opt. Express*, *16*, 3931–3948, doi:10.1364/OE.16.003931.

Cho, H.-M., S. L. Nasiri, and P. Yang (2009), Application of CALIOP measurements to the evaluation of cloud phase derived from MODIS infrared channels, *J. Appl. Meteorol. Climatol.*, *48*, 2169–2180, doi:10.1175/2009JAMC2238.1.

Chylek, P., and C. Borel (2004), Mixed phase cloud water/ice structure from high spatial resolution satellite data, *Geophys. Res. Lett.*, *31*, L14104, doi:10.1029/2004GL020428.

Chylek, P., S. Robinson, M. K. Dukey, M. D. King, Q. Fu, and W. B. Clodius (2006), Comparison of near-infrared and thermal infrared cloud phase detections, *J. Geophys. Res.*, *111*, D20203, doi:10.1029/2006JD007140.

Coakley, J. A., M. R. Friedman, and W. R. Tahnk (2005), Retrieval of cloud properties for partly cloudy imager pixels, *J. Atmos. Oceanic Technol.*, *22*, 3–17, doi:10.1175/JTECH-1681.1.

Di Girolamo, L., L. Liang, and S. Platnick (2010), A global view of one-dimensional solar radiative transfer through oceanic water clouds, *Geophys. Res. Lett.*, *37*, L18809, doi:10.1029/2010GL044094.

Doutriaux-Boucher, M., and J. Quaas (2004), Evaluation of cloud thermodynamic phase parameterizations in the LMDZ GCM by using POLDER satellite data, *Geophys. Res. Lett.*, *31*, L06126, doi:10.1029/2003GL019095.

Frey, R. A., S. A. Ackerman, Y. Liu, K. I. Strabala, H. Zhang, J. R. Key, and X. Wang (2008), Cloud detection wih MODIS. Part I: Improvements in the MODIS cloud mask for Collection 5, *J. Atmos. Oceanic Technol.*, *25*, 1057–1072, doi:10.1175/2008JTECHA1052.1.

Goloub, P., M. Herman, H. Chepfer, J. Riedi, G. Brogniez, P. Couvert, and G. Seze (2000), Cloud thermodynamical phase classification from the POLDER spaceborne instrument, *J. Geophys. Res.*, *105*, 14,747–14,759, doi:10.1029/1999JD901183.

Harshvardhan, and J. A. Weinman (1982), Infrared radiative transfer through a regular array of cuboidal clouds, *J. Atmos. Sci.*, *39*, 431–439.

Hu, Y., S. Rodier, K. Xu, W. Sun, J. Huang, B. Lin, P. Zhai, and D. Josset (2010), Occurrence, liquid water content, and fraction of supercooled water clouds from combined CALIOP/IIR/MODIS measurements, *J. Geophys. Res.*, *115*, D00H34, doi:10.1029/2009JD012384.

Jin, H., S. L. Nasiri, and B. H. Kahn (2010), Initial assessment of AIRS cloud phase determination, JP1.20, paper presented at 13th Conference on Cloud Physics and Radiation, Am. Meteorol. Soc., 28 June to 1 July 2010, Portland, Oreg.

Kahn, B. H., A. Eldering, S. A. Clough, E. J. Fetzer, E. Fishbein, M. R. Gunson, S.-Y. Lee, P. F. Lester, and V. J. Realmuto (2003), Near micron-sized cirrus cloud particles in high-resolution infrared spectra: An orographic case study, *Geophys. Res. Lett.*, *30*(8), 1441, doi:10.1029/2003GL016909.

Kahn, B. H., K. N. Liou, S.-Y. Lee, E. F. Fishbein, S. DeSouza-Machado, A. Eldering, E. J. Fetzer, S. E. Hannon, and L. L. Strow (2005), Nighttime cirrus detection using Atmospheric Infrared Sounder window channels and total column water vapor, *J. Geophys. Res.*, *110*, D07203, doi:10.1029/2004JD005430.

Kahn, B. H., A. Eldering, A. J. Braverman, E. J. Fetzer, J. H. Jiang, E. Fishbein, and D. L. Wu (2007), Toward the characterization of upper tropospheric clouds using Atmospheric Infrared Sounder and Microwave Limb Sounder observations, *J. Geophys. Res.*, *112*, D05202, doi:10.1029/2006JD007336.

Kahn, B. H., C. K. Liang, A. Eldering, A. Gettelman, Q. Yue, and K. N. Liou (2008), Tropical thin cirrus and relative humidity observed by the Atmospheric Infrared Sounder, *Atmos. Chem. Phys.*, *8*, 1501–1518, doi:10.5194/acp-8-1501-2008.

Krijger, J. M., M. van Weele, I. Aben, and R. Frey (2007), Technical note: The effect of sensor resolution on the number of cloud-free observations from space, *Atmos. Chem. Phys.*, *7*, 2881–2891, doi:10.5194/acp-7-2881-2007.

Lee, T. F., et al. (2010), NPOESS: Next-Generation Operational Global Earth Observations, *Bull. Am. Meteorol. Soc.*, *91*, 727–740, doi:10.1175/2009BAMS2953.1.

Li, Z.-X., and H. Le Treut (1992), Cloud-radiation feedbacks in a general circulation model and their dependence on cloud modeling assumptions, *Clim. Dyn.*, *7*, 133–139, doi:10.1007/BF00211155.

Liou, K.-N., and S.-C. Ou (1979), Infrared radiative transfer in finite cloud layers, *J. Atmos. Sci.*, *36*, 1985–1996, doi:10.1175/1520-0469(1979)036<1985:IRTIFC>2.0.CO;2.

Medeiros, B., B. Stevens, I. M. Held, M. Zhao, D. L. Williamson, J. G. Olson, and C. S. Bretherton (2008), Aquaplanets, climate sensitivity, and low clouds, *J. Clim.*, *21*, 4974–4991, doi:10.1175/2008JCLI1995.1.

Menzel, W. P., R. A. Frey, H. Zhang, D. P. Wylie, C. C. Moeller, R. E. Holz, B. Maddux, B. A. Baum, K. I. Strabala, and L. E. Gumley (2008), MODIS global cloud-top pressure and amount estimation: Algorithm description and results, *J. Appl. Meteorol. Climatol.*, *47*, 1175–1198, doi:10.1175/2007JAMC1705.1.

Mitchell, J. F. B., and W. J. Ingram (1992), Carbon dioxide and climate: Mechanisms of changes in cloud, *J. Clim.*, *5*, 5–21, doi:10.1175/1520-0442(1992)005<0005:CDACMO>2.0.CO;2.

Mitchell, J. F. B., C. A. Senior, and W. J. Ingram (1989), CO_2 and climate: A missing feedback?, *Nature*, *341*, 132–134, doi:10.1038/341132a0.

Morrison, A. E., S. T. Siems, and M. J. Manton (2011), A three-year climatology of cloud-top phase over the southern ocean and north Pacific, *J. Clim.*, *24*, 2405–2418, doi:10.1175/2010JCLI3842.1.

Morrison, H., and A. Gettelman (2008), A new two-moment bulk stratiform cloud microphysics scheme in the Community Atmosphere Model, Version 3 (CAM3). Part I: Description and numerical tests, *J. Clim.*, *21*, 3642–3659, doi:10.1175/2008JCLI2105.1.

Nasiri, S. L., and B. H. Kahn (2008), Limitations of bispectral infrared cloud phase determination and potential for improvement, *J. Appl. Meteorol. Climatol.*, *47*, 2895–2910, doi:10.1175/2008JAMC1879.1.

Naud, C., A. D. Del Genio, and M. Bauer (2006), Observational constraints on the cloud thermodynamic phase in midlatitude storms, *J. Clim.*, *19*, 5273–5288, doi:10.1175/JCLI3919.1.

Naud, C. M., A. D. Del Genio, M. Haeffelin, Y. Morille, V. Noel, J.-C. Dupont, D. D. Turner, C. Lo, and J. Comstock (2010), Thermodynamic phase profiles of optically thin midlatitude clouds and their relation to temperature, *J. Geophys. Res.*, *115*, D11202, doi:10.1029/2009JD012889.

Ogura, T., M. J. Webb, A. Bodas-Salcedo, K. D. Williams, T. Yokohata, and D. R. Wilson (2008), Comparison of cloud response to CO_2 doubling in two GCMs, *SOLA*, *4*, 29–32, doi:10.2151/sola.2008-008.

Oreopoulos, L., and R. F. Cahalan (2005), Cloud inhomogeneity from MODIS, *J. Clim.*, *18*, 5110–5124, doi:10.1175/JCLI3591.1.

Pavolonis, M. J. (2010), Advances in extracting cloud composition information from spaceborne infrared radiances–A robust alternative to brightness temperatures, Part 1: Theory, *J. Appl. Meteorol. Climatol.*, *49*, 1992–2012, doi:10.1175/2010JAMC2433.1.

Platnick, S., M. D. King, S. A. Ackerman, W. P. Menzel, B. A. Baum, and R. A. Frey (2003), The MODIS cloud products: Algorithms and examples from Terra, *IEEE Trans. Geosci. Remote Sens.*, *41*, 459–473, doi:10.1109/TGRS.2002.808301.

Prabhakara, C., R. S. Fraser, G. Dalu, M.-L. C. Wu, and R. J. Curan (1988), Thin cirrus clouds: Seasonal distribution over oceans deduced from Nimbus-4 IRIS, *J. Appl. Meteorol.*, *27*, 379–399, doi:10.1175/1520-0450(1988)027<0379:TCCSDO>2.0.CO;2.

Randel, D. L., T. H. Vonder Haar, M. A. Ringerud, G. L. Stephens, T. J. Greenwald, and C. L. Combs (1996), A new global water vapor dataset, *Bull. Am. Meteorol. Soc.*, *77*, 1233–1246, doi:10.1175/1520-0477(1996)077<1233:ANGWVD>2.0.CO;2.

Riedi, J., B. Marchant, S. Platnick, B. A. Baum, F. Thieuleux, C. Oudard, F. Parol, J. M. Nicolas, and P. Dubuisson (2010), Cloud thermodynamic phase inferred from merged POLDER and MODIS data, *Atmos. Chem. Phys.*, *10*, 11,851–11,865, doi:10.5194/acp-10-11851-2010.

Rossow, W. B., and R. A. Schiffer (1999), Advances in understanding clouds from ISCCP, *Bull. Am. Meteorol. Soc*, *80*, 2261–2287, doi:10.1175/1520-0477(1999)080<2261:AIUCFI>2.0.CO;2.

Schneider, T., P. A. O'Gorman, and X. J. Levine (2010), Water vapor and the dynamics of climate changes, *Rev. Geophys.*, *48*, RG3001, doi:10.1029/2009RG000302.

Schreier, M. M., B. H. Kahn, A. Eldering, D. A. Elliott, E. Fishbein, F. W. Irion, and T. S. Pagano (2010), Radiance comparisons of MODIS and AIRS using spatial response information, *J. Atmos. Oceanic Technol.*, *27*, 1331–1342, doi:10.1175/2010JTECHA1424.1.

Senior, C. A., and J. F. B. Mitchell (1993), Carbon dioxide and climate: The impact of cloud parameterizations, *J. Clim.*, *6*, 393–418, doi:10.1175/1520-0442(1993)006<0393:CDACTI>2.0.CO;2.

Stephens, G. L. (2005), Cloud feedbacks in the climate system: A critical review, *J. Clim.*, *18*, 237–273, doi:10.1175/JCLI-3243.1.

Strabala, K. I., S. A. Ackerman, and W. P. Menzel (1994), Cloud properties inferred from 8–12−μm data, *J. Appl. Meteorol.*, *33*, 212–229, doi:10.1175/1520-0450(1994)033<0212:CPIFD>2.0.CO;2.

Strow, L. L., S. E. Hannon, S. De-Souza Machado, H. E. Motteler, and D. C. Tobin (2006), Validation of the Atmospheric Infrared Sounder radiative transfer algorithm, *J. Geophys. Res.*, *111*, D09S06, doi:10.1029/2005JD006146.

Sun, Z., and K. P. Shine (1995), Parameterization of ice cloud radiative properties and its application to the potential climatic importance of mixed-phase clouds, *J. Clim.*, *8*, 1874–1888, doi:10.1175/1520-0442(1995)008<1874:POICRP>2.0.CO;2.

Tobin, D. C., H. E. Revercomb, C. C. Moeller, and T. S. Pagano (2006), Use of Atmospheric Infrared Sounder high–spectral resolution spectra to assess the calibration of Moderate resolution Imaging Spectroradiometer on EOS Aqua, *J. Geophys. Res.*, *111*, D09S05, doi:10.1029/2005JD006095.

Trenberth, K. E., and J. T. Fasullo (2010), Simulation of present-day and twenty-first-century energy budgets of the southern ocean, *J. Clim.*, *23*, 440–454, doi:10.1175/2009JCLI3152.1.

Tsushima, Y., S. Emori, T. Ogura, M. Kimoto, M. J. Webb, K. D. Williams, M. A. Ringer, B. J. Soden, B. Li, and N. Andronova (2006), Importance of the mixed-phase cloud distribution in the control climate for assessing the response of low clouds to carbon dioxide increase: A multi-model study, *Clim. Dyn.*, *27*, 113–126, doi:10.1007/s00382-006-0127-7.

Wetherald, R. T., and S. Manabe (1988), Cloud feedback processes in a general circulation model, *J. Atmos. Sci.*, *45*, 1397–1416, doi:10.1175/1520-0469(1988)045<1397:CFPIAG>2.0.CO;2.

Williams, K. D., and G. Tselioudis (2007), GCM intercomparison of global cloud regimes: Present-day evaluation and climate change response, *Clim. Dyn.*, *29*, 231–250, doi:10.1007/s00382-007-0232-2.

Winker, D. M., et al. (2010), The CALIPSO mission: A global 3D view of aerosols and clouds, *Bull. Am. Meteorol. Soc.*, *91*, 1211–1229, doi:10.1175/2010BAMS3009.1.

Wolters, E. L. A., H. M. Deneke, B. J. J. M. van den Hurk, J. F. Meirink, and R. A. Roebeling (2010), Broken and inhomogeneous cloud impact on satellite cloud particle effective radius and cloud phase retrievals, *J. Geophys. Res.*, *115*, D10214, doi:10.1029/2009JD012205.

Yang, P., H.-L. Wei, B. A. Baum, H.-L. Huang, A. J. Heymsfield, Y. X. Hu, B.-C. Gao, and D. D. Turner (2003), The spectral signature of mixed-phase clouds composed of nonspherical ice crystals and spherical liquid droplets in the terrestrial window region, *J. Quant. Spectrosc. Radiat. Transf.*, *79–80*, 1171–1188, doi:10.1016/S0022-4073(02)00348-5.

Zelinka, M. D., and D. L. Hartmann (2010), Why is longwave cloud feedback positive? *J. Geophys. Res.*, *115*, D16117, doi:10.1029/2010JD013817.

B. A. Baum, Space Science and Engineering Center, University of Wisconsin-Madison, Madison, WI 53706, USA.

B. H. Kahn, Jet Propulsion Laboratory, California Institute of Technology, 4800 Oak Grove Dr., Mail Stop 169–237, Pasadena, CA 91109, USA. (brian.h.kahn@jpl.nasa.gov)

S. L. Nasiri, Department of Atmospheric Sciences, Texas A&M University, College Station, TX 77843, USA.

M. M. Schreier, Joint Institute for Regional Earth System Science and Engineering, University of California, Los Angeles, CA 90095, USA.